ELSEVIER

Contents lists available at ScienceDirect

Materials Science & Engineering A

journal homepage: www.elsevier.com/locate/msea





Effects of Y addition on the microstructures and mechanical behavior of ZrO_xN_y/V_2O_3 -Y nano-multilayered films

Wenjie Cheng ^a, Jingjing Wang ^a, Ping Liu ^a, Xun Ma ^a, Ke Zhang ^a, Fengcang Ma ^a, Xiaohong Chen ^a, Wei Li ^a, ^{*}, Peter K. Liaw ^b

ARTICLE INFO

Keywords:
Magnetron sputtering deposition
Nano-multilayered film
Yttrium addition
Microstructure
Strengthening and toughening

ABSTRACT

 ZrO_xN_y/V_2O_3 -Y nano-multilayered films with various yttrium additions were deposited on a Si substrate by reactive magnetron sputtering technique. The influences of yttrium addition on the microstructures, strengthening, and toughening characteristics of the nano-multilayered films were examined by the X-Ray diffraction, X-ray photoelectron spectroscopy, electro-probe microanalyzer, scanning electron microscopy, transmission electron microscopy, selected area electron diffraction, and nanoindentation instrument. The experimental results showed that the template and modulation layers of the ZrO_xN_y/V_2O_3 -Y nano-multilayered films consisted of ZrO_2 , ZrON, ZrN, and V_2O_3 , Y_2O_3 , respectively. Under the role of the template layer, the modulation layer maintained the epitaxial growth, which formed a coherent interface structure between the two sublayers as a function of the yttrium addition. When the Y/VO_2 ratio was 1/2, the hardness, elastic modulus, and fracture toughness value could reach 15.1 GPa, 182.2 GPa, and 1.23 MPa m $^{1/2}$, respectively. The incorporation of yttrium atoms gave rise to the phase transition, and the coherent interface inhibited the dislocation movement during nanoindentation loading, thus contributing to the optimal mechanical behavior of the ZrO_xN_y/V_2O_3 -Y nano-multilayered films.

1. Introduction

Zirconium-based transition metal nanofilms are widely used as hard protective films for stamping machines, instruments, cutting tools, mold parts, etc. [1] because of their excellent properties, such as high hardness [2–5]. However, the relatively weak brittleness of nanofilms with increasing hardness causes cracks and delamination, reducing the service life of the equipment. Exploiting superior nanofilms with high strength and toughness has become a common concern for researchers [6].

Several processes can be used to improve the properties of the nanofilms, such as multilayer structures [7], dropping metal phases [8–10], phase transformation [11,12], and introducing appropriate stresses [13–15]. Among them, dropping the metal phase is the most popular method to improve the properties because of its considerable operability, industrial scalability, and ability to achieve dense coatings with flat and planar surfaces [16]. For example, the yttrium (Y) addition has been extensively investigated. Mo et al. [17] investigated the

influence of multilayer modulation and elemental Y-addition on the microstructure, corrosion behavior, and oxidation resistance properties of AlTiN coatings. The results showed that adding 0.97 atomic percent (at.%) Y refined the grain size and compacted the microstructure in the AlTiN/AlTiYN multilayer coatings, significantly improving oxidation and corrosion resistance. Liu et al. [18] obtained the nano-multilayered CrN/AlN coatings at various Y contents in a magnetron sputtering deposition system. It showed that the coatings with a lower Y content had considerable wear performance, while the wear properties of the coatings declined as the Y content increased. By cathodic-arc evaporation, Tian et al. [19] deposited the CrAlYN coatings at various Y additions (0, 5, and 12 at.%). The doping of 5 at.% Y into CrAlN postponed the formation of w-AlN, which elevated the hardness value after annealing. However, alloying of Y negatively affected the oxidation resistance of CrAlN. Ye et al. [20] investigated the microstructure of W-Y-N coatings with Y additions ranging from 0 to 8.2% using reactive magnetron sputtering. The results revealed that Y atoms replaced W atoms to form the W-Y-N solid-solution coatings, which showed a

E-mail address: liwei176@usst.edu.cn (W. Li).

^a School of Materials and Chemistry, University of Shanghai for Science and Technology, Shanghai, 200093, PR China

b Department of Materials Science and Engineering, The University of Tennessee, Knoxville, TN, 37996, USA

^{*} Corresponding author.

single-phase face-centered cubic (FCC) structure with a shift in the preferred orientation from (200) to (111). The solid solution strengthening and grain refinement enhanced the hardness of the coating by the addition of Y. Meanwhile, the resistance to the elastic strain and plastic deformation of the coatings had also been improved. The zirconium-hydride alloy films with different Y contents using magnetron sputtering were studied by Han et al. [21]. It showed that more grain-boundary defects were formed in the zirconium hydride matrix due to the introduction of the Y atom, which improved the hardness and elastic modulus of zirconium hydride alloy films. A simple solid-solution treatment method for the preparation of the HfO2 dielectric films with Y doping was reported by Liang et al. [22]. These Hf-Y-O films had excellent cost-effectiveness and dielectric properties, which were applied to various thin-film transistor components. Consequently, the Y addition significantly affected nanofilms' characteristics, microstructures, and mechanical properties. Nevertheless, The Y element's mechanism, chemical state, and mechanical behavior in modulation layer of nano-multilayered films had not been reported.

Magnetron sputtering is a non-thermal evaporation process that ejects the atoms from the target surface by the momentum transfer of atomic-sized high-energy bombarding particles. Therefore, the substrate will not deform because of the excessive deposition temperature. Direct current (DC) cathode is mainly applied for sputtering metal materials. Nevertheless, radio frequency (RF) cathode can deposit almost all materials, which confine the motion of secondary electrons near the target surface by a magnetic field, including conductors, semiconductors, and insulators [23–25]. Two alternating layers form the nano-multilayered film, usually of different thicknesses. The thicker one is termed the "main layer", also named the "template layer," and the thinner is reported as the "modulation layer." The structure and properties of the nano-multilayered film depend on the main layer, yet the modulation layer can also significantly impact the film through the structural transformation.

In the present work, the Zr metal (99.99% purity) with a hexagonal close-packed (HCP) structure is selected for the template layer. The VO₂ compound (99.99% purity) with distorted rutile (<70 °C, monoclinic) structure and the Y metal (99.99% purity) with an HCP structure are selected for the modulation layer. A series of the ZrO_xN_y/V₂O₃-Y nanomultilayered films with different Y additions will be synthesized by the magnetron sputtering technique. The influence of VO₂/Y in the modulation layer on its fracture toughness is examined by studying the microstructures and mechanical behavior of the nano-multilayered films. Furthermore, the correlation among deposition parameters, microstructures, and mechanical behavior are also discussed.

2. Experimental method

2.1. Films deposition

The ${\rm ZrO_xN_y/V_2O_3}$ -Y nano-multilayered films were manufactured using reactive magnetron sputtering (JGP-450), as shown in Fig. 1. Zr metal was installed at the DC cathode target position, meanwhile

different ratios of VO₂/Y were fitted at the RF cathode target position. The VO₂ powder metallurgy and Y metal were cut into 15 pieces to fabricate the VO₂-Y compound target with different VO₂ and Y contents. The volume ratio of Y/VO₂ was set at 0/15, 1/14, 2/13, 3/12, 4/11, 5/ 10, and 6/9, respectively. The nano-multilayered films with different Y additions were deposited on the 10 \times 20 \times 0.65 mm^3 silicon (100) substrate. After ultrasonically cleaning the substrate in acetone and ethanol for 20 min, it was dried in N2 (99,9999%, volume percent) and held on a substrate holder. The target was placed at a distance of 50 mm from the substrate. The power of DC mode and RF mode were set to 160 W and 100 W, respectively. Vacuum was drawn to 4 \times $10^{\text{--}3}$ Pa, and Ar (99.9999%, volume percent) was injected before deposition. For 15 min, the target was etched with Ar ions to remove surface impurities. Thicknesses of the template layer and modulation layer were controlled by the dwell time of the silicon substrate on the target, respectively, 15 s and 8 s. The substrate rotation speed was set to 3.8 rpm. N2 and Ar gases were introduced into the chamber through a separate flow controller.

2.2. Characterization and test

The X-ray diffraction [XRD, Bruker D8 Advance Diffractometer, Cu K_{α} radiation (wavelength = 0.1542 nm)] characterized the crystal structures of the ZrO_xN_v/V₂O₃-Y nano-multilayered films. The scanning angle range was from 20 to 80°. The electron probe micro analyzer (EPMA, JXA-8530F PLUS) with an accelerating voltage of 15 kV analyzed the elemental contents. The X-ray photoelectron spectroscopy (XPS, Thermo Fisher Scientific K-Alpha) characterized the bonding states and chemical compositions. The microstructures of the nanomultilayered films were characterized using scanning electron microscopy (FE-SEM, FEI Quanta FEG 450), high-resolution transmission electron microscopy (HRTEM, FEI TECNAI F30) and selected area electron diffraction (SAED). The Bruker TI-980 Nano indenter with Berkovitch cone diamond tip was used to evaluate the hardness and toughness of the ZrO_xN_v/V_2O_3 -Y nano-multilayered films. The penetration depths were 100 nm and 4/5 thickness, respectively, avoiding the influence of the substrate. During the hardness test, six matrix indentations with a spacing of about 30 µm were carried out on the surface of each film sample. Average hardness and elastic modulus were evaluated from load-displacement curves using Oliver and Pharr methods [26]. the penetration depth was selected as 100 nm, which was less than 1/10 of the film thickness, and the drift rate was less than 0.05. The maximum load of the indenter was $13 \,\mu N$. In the toughness evaluation of nano-multilayered films, the indenter was selected at a 10 N maximum load, and the penetration depth was 4/5 of nano-multilayered films thickness, which made the surface show an obvious crack and minimized the influence of the substrate on the loading force.

3. Results

3.1. Microstructure and morphology

Fig. 2 shows the XRD patterns of the ZrO_xN_y/V₂O₃-Y nano-

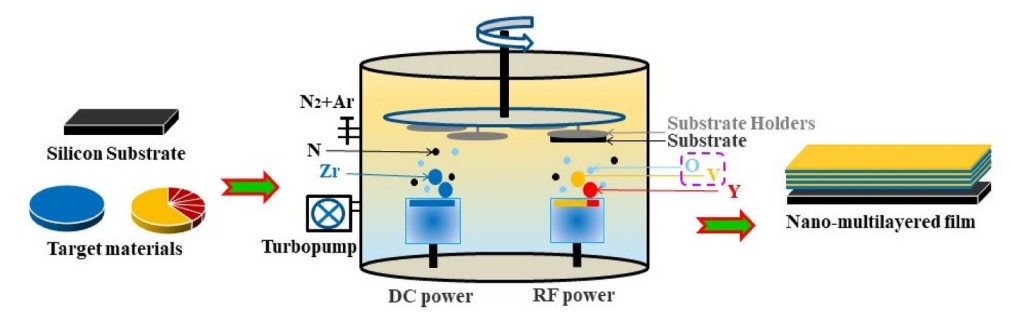


Fig. 1. Schematic diagram of a high vacuum dual cathode magnetron sputtering system.

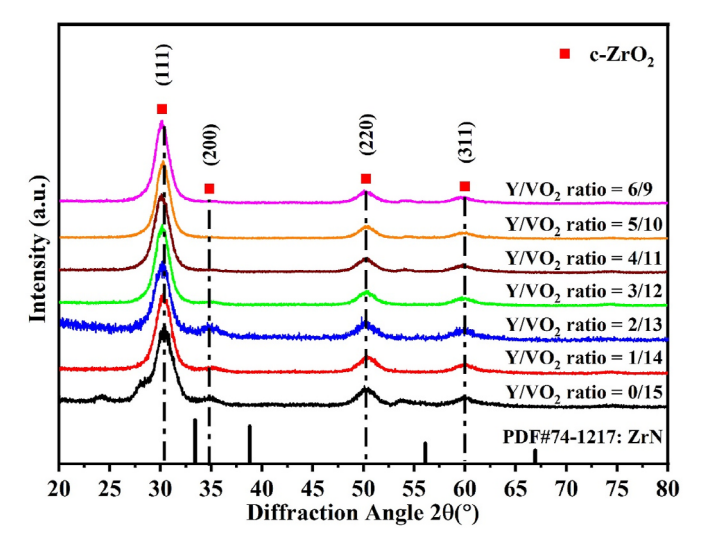


Fig. 2. XRD patterns of ${\rm ZrO_xN_y/V_2O_3}$ -Y nano-multilayered films with different Y/VO $_2$ ratios.

multilayered films. All the ZrO_xN_v/V₂O₃-Y nano-multilayered films exhibit a typical FCC structured ZrO₂, showing a strong (111) preferred orientation with relatively weak (200), (211), and (311) peaks. The intensity of the (111) diffraction peak gradually becomes stronger with an initial increase of the Y content when the Y/VO2 ratio is 5/10. It suggests that the crystallinity of the ZrO_xN_v/V₂O₃-Y nano-multilayered films is improved. Meanwhile, the full width at half maximum of the diffraction peak gets progressively narrower, showing the grain size grew continuously. During the growth of ZrO_xN_v and V₂O₃-Y sublayers, the incorporation of Y partially replaces the smaller V atoms in the V-O lattice, increasing the lattice constant, and the (111) primary diffraction peaks of the ZrO_xN_v/V₂O₃-Y nano-multilayered films shift to lower angles in XRD with the Y addition, which indicts the existence of intrinsic compressive residual stress in the nano-multilayered films. The stressfield variations affect the lattice parameters and mechanical properties of the nano-multilayered films [27]. Besides, the deposition time of the substrate is shorter in RF mode, and the lower sputtering power might be the main reason for the absence of modulation-layer phases in the XRD spectra.

Based on the XRD results, the Bragg's law [28] was used to calculate the interplanar spacing of the crystal, d, from the (111) diffraction peaks.

$$d = \frac{n\lambda}{2 \cdot \sin \theta} \tag{1}$$

in which n (an integer) is the "order" of reflection, λ is the wavelength of the incident X-rays, and θ is the angle of incidence.

The lattice parameters are obtained by Equation (1). The d of the nano-multilayered films increases from ~ 2.94 to ~ 2.97 Å with increasing Y content, as shown in Fig. 3. The relationship between d and Y content is approximately linear. The d expansion is attributed to the replacement of V atoms by larger Y atoms in the V_2O_3 lattice [29,30].

Following the Scherrer formula [31], the grain size of the nano-multilayered films is evaluated by the XRD with the full width at half maximum (FWHM) values of the (111) peaks.

$$D_{hkl} = \frac{K\lambda}{\beta \bullet \cos \theta} \tag{2}$$

where D_{hkl} is the grain size, K is generally chosen to be 0.94 when the crystal is cubic symmetric, λ is the wavelength of the Cu K_a radiation 1.5406 Å, and β is the full width at half maximum of the (111) peak height.

In Fig. 3, the full width at half maximum of the (111) diffraction peak

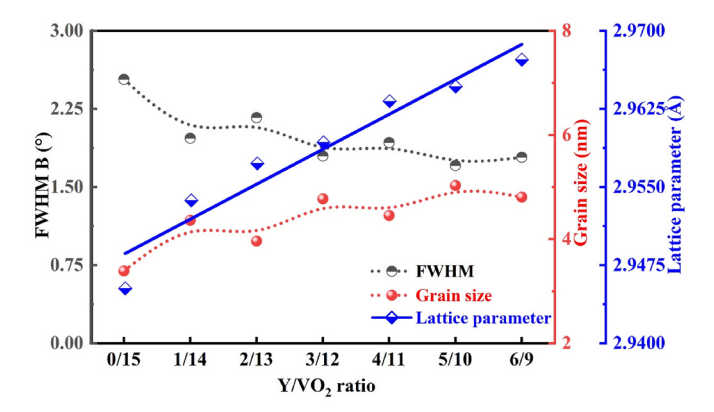


Fig. 3. The full width at half maximum, average grain size, and lattice parameters of the ZrO_xN_v/V_2O_3 -Y nano-multilayered films for the Y/VO_2 ratios.

gradually becomes narrower and then wider with increasing the Y content. The minimum value reaches 1.708° when the Y/VO_2 ratio is 5/10. Correspondingly, as the Y/VO_2 ratio changes from 0/15 to 5/10, the grain size of nano-multilayered films increases from ~ 3.4 nm to ~ 5.0 nm. The Y addition can grow grain size [32], suggesting that the nano-multilayered films gradually improve crystallinity. When the Y/VO_2 ratio is further increased to 6/9, the grain size is reduced to 4.8 nm, resulting in Y nanoclusters separating from supersaturated V-Y-O grains, together with its effect on the grain refinement of ZrO_xN_y layers [30,33].

The elemental contents of the ZrO_xN_y/V_2O_3 -Y nano-multilayered films are shown in Fig. 4. The chemical composition of the nano-multilayered films is not stoichiometric. As the Y/VO_2 ratio increases, N, Zr, and O contents remain stable at 1.4, 26.0, and 69.9 at.%, respectively. The V content decreases as the Y content increases. When the Y content changes from 0 to 1.5 at.%, the V content drops from 3.3 to 0.7 at.%, which can be explained by increasing the Y/VO_2 ratio in the target during the deposition.

The XPS can illustrate the production of the compound phase. Fig. 5 presents the Zr 3d, V 2p, and Y 3d spectra of the ZrO_xN_y/V_2O_3 -Y nanomultilayered film for the Y/VO_2 ratio of 5/10. It is chosen as representative owing to its superior mechanical properties. The mixed peak of metal oxides is identified on the O 1s spectrum at 530.6 eV [34,35], as

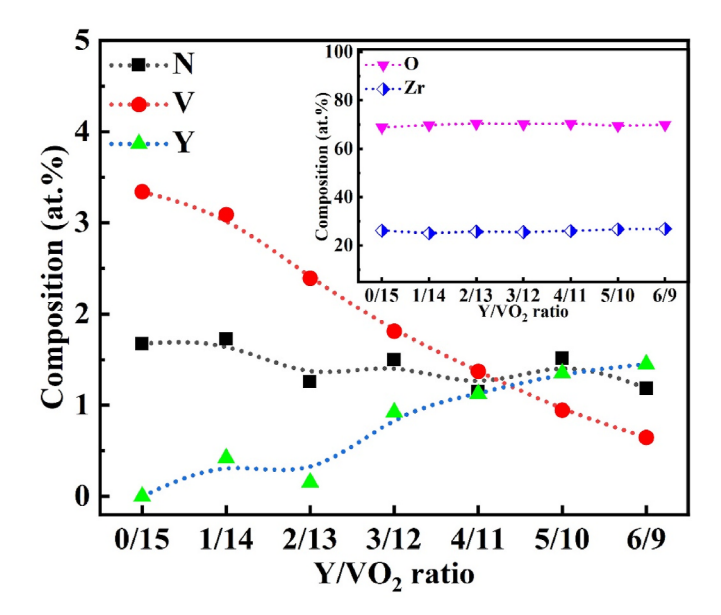


Fig. 4. Chemical composition of ${\rm ZrO_xN_y/V_2O_3\text{-}Y}$ nano-multilayered films with different Y/VO $_2$ ratios.

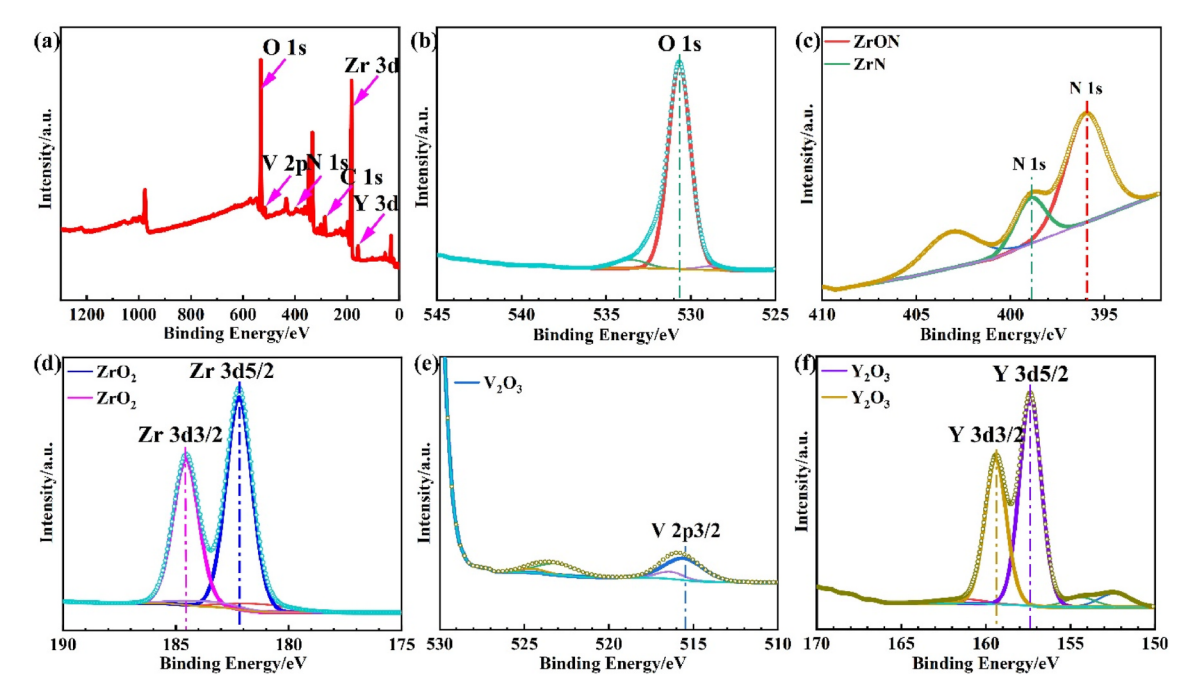


Fig. 5. (a) Survey XPS spectra for ZrO_xN_y/V_2O_3 -Y nano-multilayered film with Y/VO_2 ratio 5/10, high-resolution XPS spectra of (b) O 1s, (c) N 1s, (d) Zr 3d, (e) V 2p, (f) Y 3d.

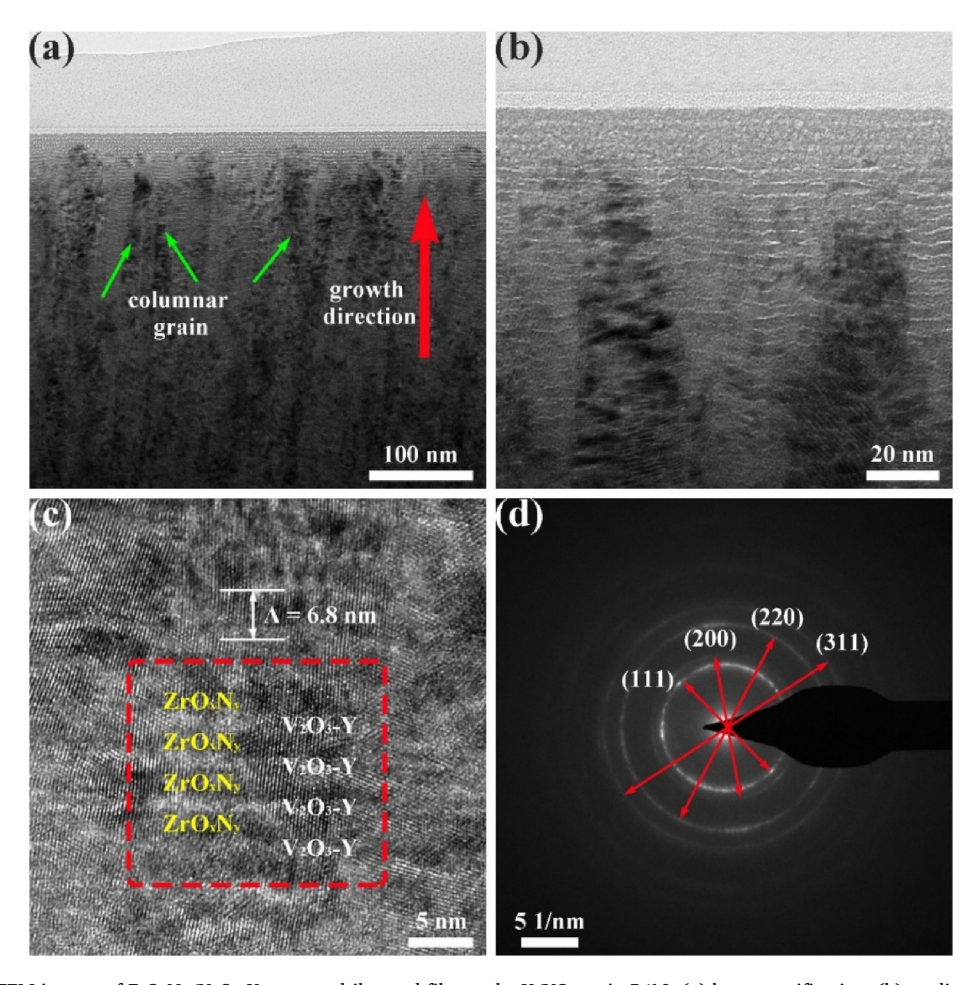


Fig. 6. Cross-sectional TEM images of ZrO_xN_y/V_2O_3 -Y nano-multilayered film as the Y/VO2 ratio 5/10. (a) low-magnification, (b) medium-magnification, (c) high-magnification, and (d) selected area diffraction patterns.

shown in Fig. 5(b). For the N 1s spectrum, the two components in Fig. 5 (c) can be fitted. The peak at 398.9 eV corresponds to the ZrN bond [35, 36]. The peak at the lower energy side near 396.3 eV belongs to the Zr (N, O)-like structure [35,37]. The Zr 3d peaks are fitted as paired spin-orbit splitter peaks, separating the Zr 3d5/2 and Zr 3d3/2 components by 2.4 eV in Fig. 5(d). The spectrum shows two stable peaks as binding energies of 182.18 and 184.58 eV, which correspond to the Zr 3d3/2 and Zr 3d3/2 components of the ZrO₂, respectively [32,38]. The V 2p3/2 peak for the film located at about 515.7 eV, as shown in Fig. 5 (e), is characteristic of V³⁺, which is recognized as a V-O bond corresponding to V₂O₃ [39,40]. There is a 2.0 eV separation of the Y 3d peak between the Y 3d3/2 and Y 3d3/2 components in Fig. 4(f) the peak at 157.0 eV attributes to Y 3d5/2, and the peak at 159.0 eV belongs to Y 3d3/2. The two peaks are the characteristic signals of the components of Y_2O_3 [40,41]. In summary, the constituent phases of the ZrO_xN_v/V_2O_3-Y nano-multilayered films can be identified as ZrO2, ZrON, ZrN, V2O3, and Y₂O₃ by XPS studies.

Variations in the Ar ions sputtering yields of the elements contribute to the different phase compositions of the nano-multilayered films [42]. VO_2 is one type of low-temperature phase transition material [43,44]. Under the influence of Ar ion bombardment and chamber temperature, V and O ions are separated from unstable VO_2 , which results in a stable V_2O_3 phase at the RF target. Furthermore, the V_2O_3 content gradually reduces while the Y_2O_3 content grows as the Y addition increases, and the Y atoms are doped into the V_2O_3 lattice at the atomic-metal sites. When the substrate is located at the DC target, the zirconium oxide is preferentially formed in the nano-multilayered film because the affinity of O for Zr is higher than that of N [45,46]. Therefore, the phase content of the template layer is $ZrO_2 > ZrON > ZrN$.

Fig. 6 presents the TEM and SAED of the ZrO_xN_v/V₂O₃-Y nanomultilayered film with the Y/VO_2 ratio of 5/10. The columnar grain structure is observed in the cross-sections of the nano-multilayered film in Fig. 6(a). The average grain size is approximately 4.4 nm, consistent with the calculated values from XRD. The distinct layered structure of the nano-multilayered film is presented in Fig. 6(b). The nano-layered structures with dark and bright contrasts represent the ZrOxNv and V₂O₃-Y sublayers. It is evident from Fig. 6(c) that the lattice fringes remain clear from one modulation layer to the next, indicating that most V₂O₃-Y grains are epitaxially grown on the ZrO_xN_v sublayer. The lattice fringes pass through several sublayers and interfaces, which show that the modulation layers are fully transformed into FCC structures and form coherent interfaces with the template layers. The growth of interface coherent in the ZrO_xN_v/V_2O_3 -Y nano-multilayered films is associated with the thermodynamic energy balance between the interfacial energy and the coherent strain, which is driven by the minimization of interfacial energy [35,47]. The microstructural evolution of V₂O₃-Y sublayers in ZrO_xN_v/V₂O₃-Y nano-multilayered films with the increase in Y/VO2 ratio can be explained by a thermodynamic model. The total energy (E_T) of V₂O₃-Y sublayer is composed of strain-free bulk energy (E_{bulk}), strain energy (E_{str}), and interfacial energy (E_{int}), which can be written as [48],

$$E_T = E_{bulk} + E_{str} \bullet Y\% + E_{int} \tag{3}$$

in which E_{bulk} is a constant. During the initial increase of Y/VO₂ ratio (less than 5/10), E_{int} is the main component of E_T . Formation of the coherent interface between $\operatorname{ZrO_xN_y}$ and $\operatorname{V_2O_3-Y}$ sublayers can lower E_{int} . Therefore, $\operatorname{V_2O_3-Y}$ sublayers can transform into FCC structure and grow epitaxially with $\operatorname{ZrO_xN_y}$ sublayers, as shown in Fig. 6(c). When Y/VO₂ ratio rises to 6/9, the E_{str} increase, which occupy a larger proportion in E_T than E_{int} . E_T cannot be reduced by forming a coherent interface. Therefore, the epitaxial growth of V₂O₃-Y sublayers may not maintain with $\operatorname{ZrO_xN_y}$ sublayers. The continuous SAED patterns in Fig. 6(d) can be identified as typical FCC structures with (111), (200), (220), and (311) orientations, confirming the presence of the FCC polycrystalline phases in the $\operatorname{ZrO_xN_y/V_2O_3-Y}$ nano-multilayered films. Thus, the SAED tests are

compatible with XRD results. The average modulation period is approximately 6.8 nm, which is compatible with the estimated value of the nano-multilayered film thickness divided by the total number of periods.

The index of the fragment displayed in Fig. 6(c) is implemented using the fast Fourier transform (FFT), as shown in the square area box in Fig. 7(a). After filtering, the image of the reciprocal lattice points corresponds to the grains with the direction of (111). The interplanar distance, d, calculated is 2.957 Å, consistent with the calculations from the previous XRD. Fig. 7(b) demonstrates the perfect lattice match between the ZrO_xN_y and the V_2O_3 -Y sublayers. The epitaxial interface between the two sublayers is in the filtered inverse fast Fourier transform (IFFT) image of Fig. 7(d). The IFFT spectra confirm the stability of the FCC phase in the nano-multilayered films, which is compatible with the XRD results, and it further indicates that the interlayer lattice constants are closely matched [49]. Furthermore, the dislocations with the extra half-plane atoms at the interfaces between the V_2O_3 -Y and ZrO_xN_y sublayer can improve the local stability of the coherent interfaces [35, 50], in Fig. 7(d).

Fig. 8 provides cross-sectional images of the ZrO_xN_y/V_2O_3 -Y nanomultilayered films due to various Y additions. It exhibits a distinct columnar and dense grain structure, independent of the Y addition and nano-multilayered architecture. The cross-sections and surfaces show no apparent defects. The average thickness of the ZrO_xN_y/V_2O_3 -Y films is about 1,050 \pm 90 nm with a variety of V_2O_3/Y ratios.

3.2. Hardness and modulus

Fig. 9 shows the hardness and elastic modulus of the ZrO_xN_y/V_2O_3 -Y nano-multilayered films as a function of the Y/VO_2 ratios. As the Y/VO_2 ratio increases, the hardness and elastic modulus of the nano-multilayered films increase first and then reduce. All the ZrO_xN_y/V_2O_3 -Y nano-multilayered films exhibit higher hardness and elastic modulus than the ZrO_xN_y/V_2O_3 nano-multilayered film. The maximum hardness and elastic modulus values of the ZrO_xN_y/V_2O_3 -Y nano-multilayered film reach 15.1 and 182.3 GPa, respectively, at the Y/VO_2 ratio is 5/10. When the Y/VO_2 ratio is further increased to 6/9, the hardness and elastic modulus of the nano-multilayered film are reduced, which can be attributed to the fact that the coherent interfacial structure is no longer maintained [51,52].

3.3. Toughness

The plastic deformation relates to H^3/E^2 , the elevated H^3/E^2 values indicate the improving ability of the nano-multilayered films to absorb energy during the deformation to fracture period. The elastic strain to failure associated with H/E may be utilized to characterize the resistance of the nanofilms to cracking, higher H/E values reveal that the nanomultilayered films have better wear resistance. which are related to the toughness of the nanofilms [35,53–55].

Fig. 10 shows the H/E and H^3/E^2 ratios of the $\rm ZrO_xN_y/V_2O_3$ -Y nanomultilayered films with different $\rm Y/VO_2$ ratios. The result exhibits that the variation tendencies of H/E and H^3/E^2 ratios are the same as that of hardness, increasing first and then decreasing. When the $\rm Y/VO_2$ ratio is 5/10, the nano-multilayered films obtain the most significant H/E and H^3/E^2 values with 0.079 and 0.093 GPa, respectively. It manifests that the $\rm ZrO_xN_y/V_2O_3$ -Y nano-multilayered films with high hardness and excellent fracture toughness can be obtained simultaneously by optimizing Y addition.

4. Discussion

4.1. Strengthening mechanism

Nanoindentation experiments on the ZrO_xN_y/V_2O_3 -Y nanomultilayered films reveal that the microstructures substantially affect

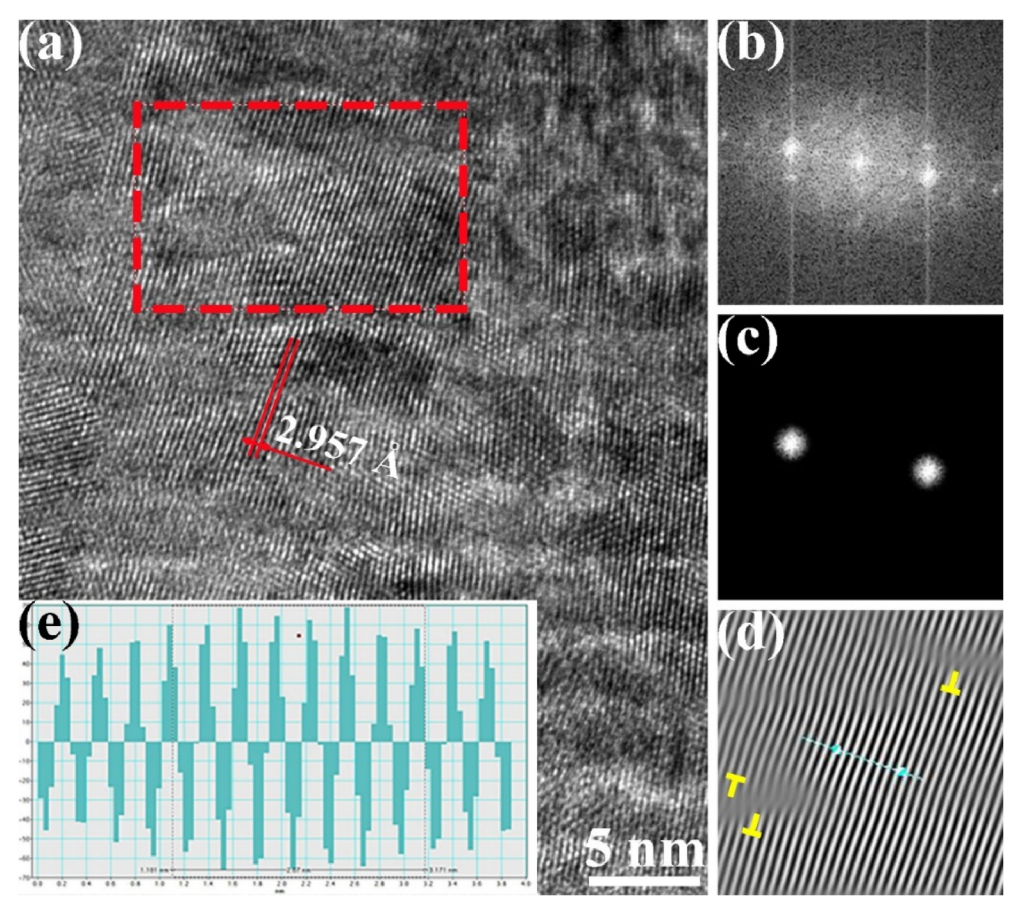


Fig. 7. As the Y/VO_2 ratio is 5/10, the high-resolution TEM images of the ZrO_xN_y/V_2O_3 -Y nano-multilayered film (a) with the corresponding FFT pattern (b), inverse FFT image(c), after applying mask (d), and profile of the inverse FFT image (e).

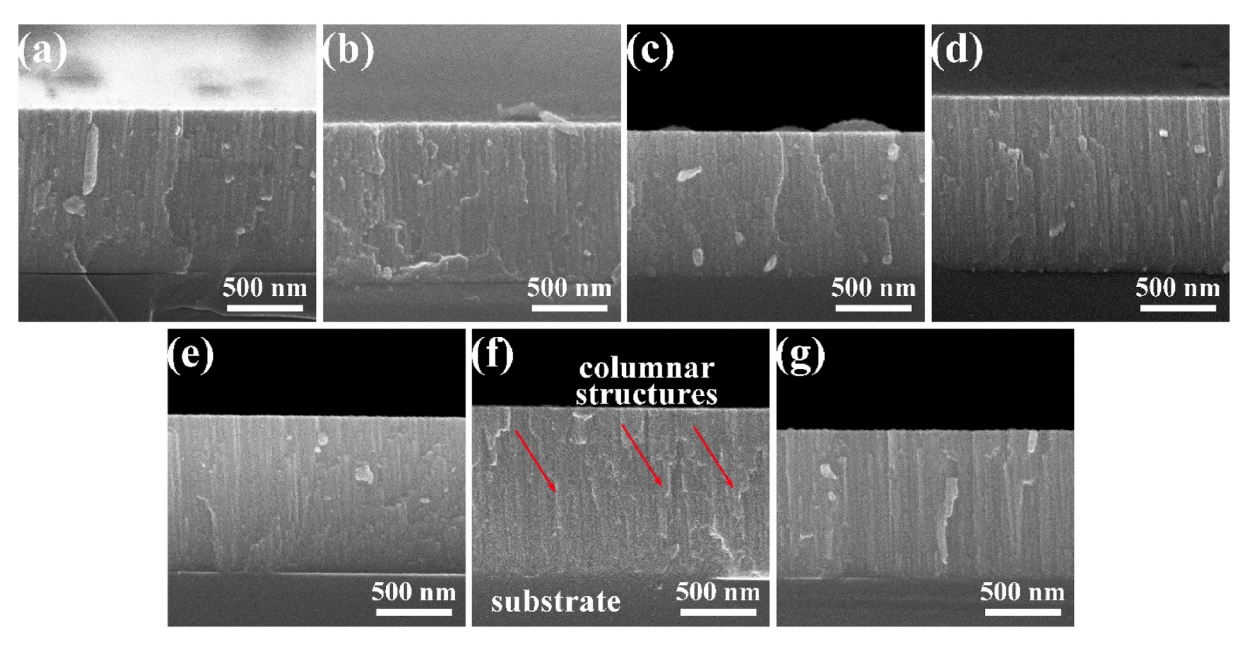


Fig. 8. Morphology of the cross-sections observed in SEM for ZrO_xN_y/V_2O_3 -Y nano-multilayered films deposited with various Y/VO_2 ratios. (a) 0/15, (b) 1/14, (c) 2/13, (d) 3/12, (e) 4/11, (f) 5/10, (g) 6/9.

the mechanical properties. When the Y/VO₂ ratio is 5/10, the mechanical properties of the nano-multilayered film enhanced by nanoscale multilayered structures are extensively studied in Koehler's model [56], Hall-Petch strengthening [57], and alternating stress field effects

[58].

As the Y/VO₂ ratio is below 5/10, the V_2O_3 -Y sublayers exhibit FCC structure under the "template effect" and grow epitaxially with the ZrO_xN_y sublayers. When the dislocations traverse through the coherent

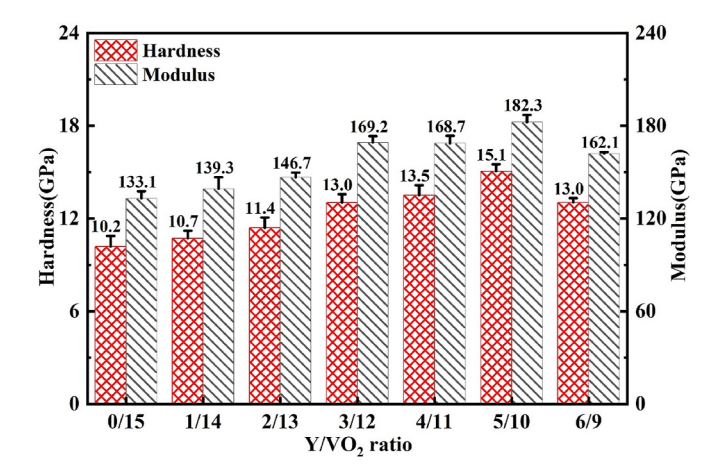


Fig. 9. The hardness and elastic modulus for the ZrO_xN_y/V_2O_3 -Y nanomultilayered films with various Y/VO_2 ratios.

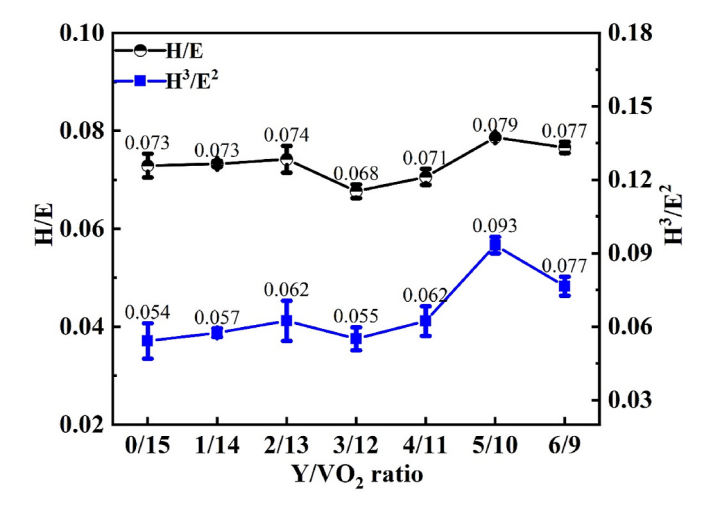


Fig. 10. The H/E and $\rm H^3/E^2$ ratios of $\rm ZrO_xN_y/V_2O_3\text{-}Y$ nano-multilayered films with the various $\rm Y/VO_2$ ratios.

interface in nano-multilayered film, they are hindered at interfaces by the forces generated from the two sublayers with different shear moduli. The larger the difference between the shear moduli of two sublayers, the more obvious the additional stress blocks the dislocation motion and the more significant the nano-multilayered film's strengthening effect. The shear modulus of ZrO2, V2O3, and Y are about 81, 67, and 60 GPa, respectively [59,60]. With the increase of Y addition, the shear modulus of V₂O₃-Y continuously decreases, increasing the shear modulus difference between the two adjacent sublayers. Meanwhile, the crystallinity of the nano-multilayered films increases, as shown in Fig. 2. Furthermore, the alternating stress field is formed in the nano-multilayered film due to the Y atoms substituting the V atoms in the V₂O₃ lattice. Consequently, the ZrO_xN_y/V₂O₃-Y nano-multilayered films can be gradually strengthened. When the Y/VO2 ratio is further increased to 6/9, the amount of Y₂O₃ phase in the V₂O₃-Y sublayer increases, while the content of the V₂O₃ phase decreases. As a result, the co-epitaxial growth structure between ZrO_xN_v and V₂O₃-Y sublayers is damaged. The hardness and elastic modulus are significantly reduced to 13.0 GPa and 162.1 GPa, respectively.

4.2. Toughness evaluation

The fracture toughness or the critical stress intensity factor is named K_{IC} . The fracture toughness of the ZrO_xN_y/V_2O_3 -Y nano-multilayered

films can be further evaluated by the following Equation [61]:

$$K_{IC} = \delta \left(\frac{E}{H}\right)^{\frac{1}{2}} \left(\frac{P}{c^{\frac{3}{2}}}\right) \tag{4}$$

in which K is the stress intensity factor entirely, I is the mode I fracture with cracking opening under tensile forces, $\delta=0.016$ (Berkovich type), c (μ m) is the average value of the radial crack lengths, which is measured nine times. The maximum and minimum values are removed, and the mean and standard deviation are calculated for the remaining seven values. P (mN) is the maximal load. H and E are hardness and modulus values. The fracture occurs when the stresses or strains at the crack tip reach a critical value, K_{IC} .

As the Y/VO₂ ratio increases, the c value of the ZrO_xN_v/V_2O_3 -Y nanomultilayered films present in Fig. 11. The shortest c value is 3.37 μ m when the Y/VO₂ ratio is 0/15, indicating that the ZrO_xN_y/V₂O₃-Y nanomultilayered film may exhibit good toughness. In fact, the results display poor resistance to damage due to the lower hardness. When the Y/VO₂ ratio increases to 5/10, the c value is shorter, and the nano-multilayered film has better fracture toughness. As the Y/VO₂ ratio reaches 6/9, the c value is increased, and the fracture toughness of the nano-multilayered film deteriorates. Fig. 11(h) shows the load-displacement local amplification curve of the ZrO_xN_v/V₂O₃-Y nano-multilayered film as the Y/ VO₂ ratio is 5/10. During the initial loading stage, the load increases smoothly, slowly, and continues to grow as the displacement increases, demonstrating the uniform and dense microstructures of the nanomultilayered films. At a load of about 137 mN and a displacement of 758 nm, there is a discontinuous step in the indenter motion caused by a "pop-in" event of the indenter into the material [62]. This nanoscale deformation in the ZrO_xN_v/V₂O₃-Y nano-multilayered film may be attributed to dislocation nucleation and propagation [63].

In Fig. 12, the K_{IC} values calculated from Equation (4) are 0.72, 0.66, 0.64, 0.76, 0.71, 1.29, and 0.64 MPa m^{1/2}, respectively. The K_{IC} values generally elevate first and then reduce as the Y/VO2 ratio increases. The maximum K_{IC} value is 1.23 MPa m^{1/2}, as the Y/VO₂ ratio is 5/10. It is approximately two times that of the nano-multilayered film with the Y/ VO2 ratio of 2/13. In our previous study, the ZrOxNv/V2O3 nanomultilayered films exhibited a maximum fracture toughness of 0.88 MPa $m^{1/2}$ [64]. It indicated that the ZrO_xN_y/V_2O_3 -Y nano-multilayered films had excellent toughness and previously confirmed the values of H^3/E^2 and H/E. Kainz et al. [65] investigated the mechanical behavior of TiN/TiBN nano-multilayered films. The fracture toughness increased from 2.2 MPa $m^{1/2}$ for TiN to 5.0 MPa $m^{1/2}$ for TiBN with the addition of appropriate boron. The improved fracture toughness of TiBN was connected with the existence of additional boron phases and grain refinement. In the a-CuZr/c-ZrN system with thicknesses of 25/46 nm, the optimal fracture toughness was 0.55 MPa m^{1/2} (about 43% higher than the ZrN single-layer film) [66]. Ren et al. [54] evaluated the strengthening-toughening behavior of the Ag/TaC nano-multilayered films. The results showed that the soft Ag layers induced deformation and crack bridging, improving the nano-multilayered film's fracture toughness. These researches indicate that the beneficial ductile properties of metals, either as modulation layers or as constituent elements in modulation layers, would contribute to the fracture toughness of the nano-multilayered films. The K_{IC} value reduces to 0.64 MPa m^{1/2} with the Y/VO2 ratio further increasing to 6/9, showing that the nano-multilayered films' fracture toughness has been damaged.

The crack deflection increases the fracture-energy consumption and reduces the crack-propagation path during crack propagation. The crack bridge connects the two surfaces of the crack and generates tensile stresses between the two interfaces, leading to crack closure [67,68]. Fig. 13 shows the enlarged crack-tips morphology of the $\rm ZrO_xN_y/V_2O_3-Y$ nano-multilayered films in Fig. 11. The white dashed line indicates the crack expansion path, the crack bridge is located in the yellow oval area, and the arrow points to the place of the crack deflection. It can be observed that the radial cracks all exhibit a zigzag propagation path in

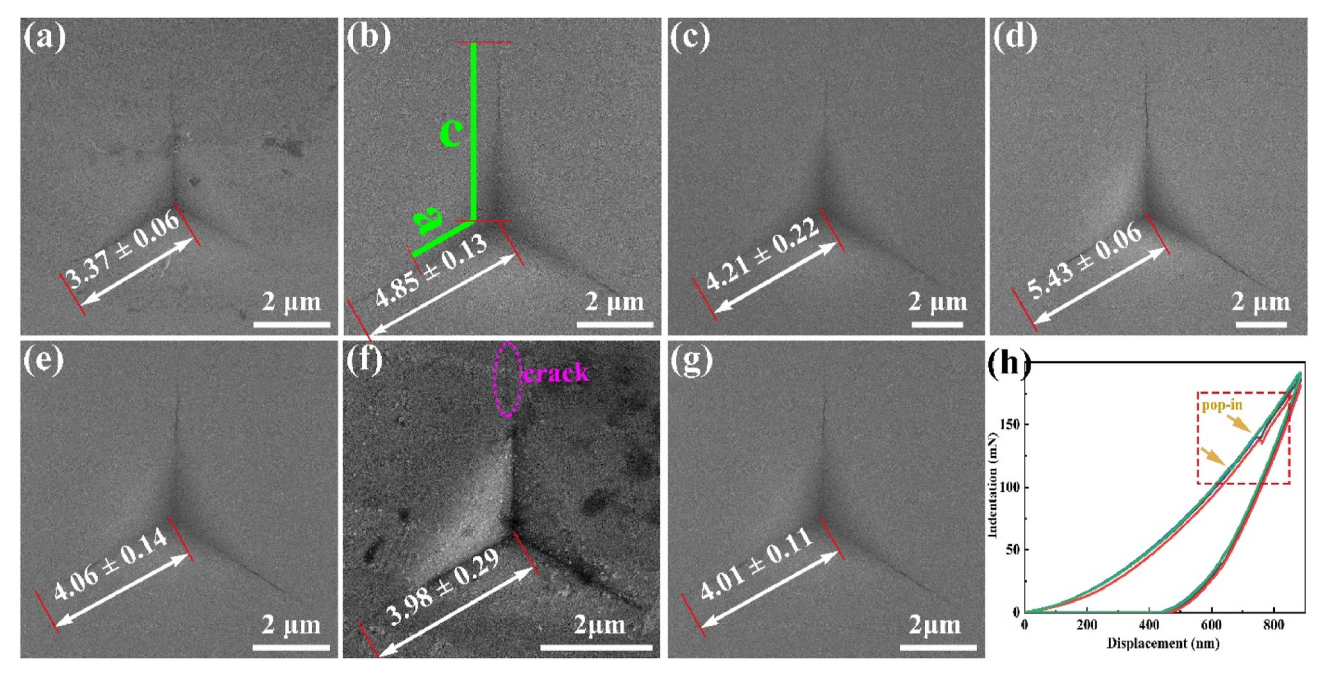


Fig. 11. SEM image of indentation-induced cracking for the ZrO_xN_y/V_2O_3 -Y nano-multilayered films with the Y/VO_2 ratio of (a) 0/15, (b) 1/14, (c) 2/13, (d) 3/12, (e) 4/11, (f) 5/10, (g) 6/9, and (h) in the dashed rectangle, arrows point to the discontinuity in the curve-loading section of (f).

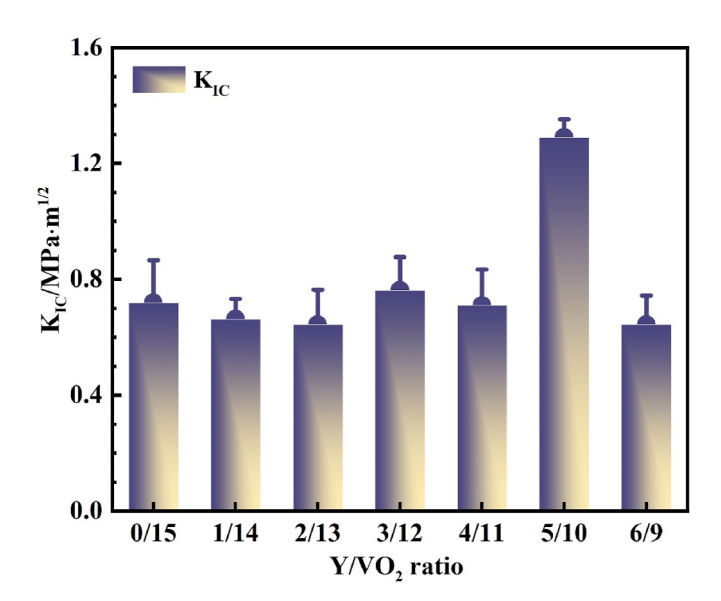


Fig. 12. Fracture toughness of the ${\rm ZrO_xN_y/V_2O_3\text{-}Y}$ nano-multilayered films with the various ${\rm Y/VO_2}$ ratios.

the nano-multilayered films. In Fig. 13(a) and (c) enlarged areas, crack bridging and crack deflection could be distinguished. More interface cracks bridging and crack deflection are noticed when the Y/VO_2 ratio is 5/10, in Fig. 13(f). These effects effectively enhance the fracture toughness of the nano-multilayered films [69].

The fracture-toughening mechanisms of the ${\rm ZrO_xN_y/V_2O_3}$ -Y nanomultilayered films can be explained as follows. Crack bridging and crack deflection will consume the crack propagation energy, thus improving the fracture toughness of the films [70]. In addition, fracture toughening has significant similarities with hardening in mechanism [71]. Hall-Petch strengthening controls fine grain hardening and improves the fracture toughness of the nano-multilayered films [72].

5. Conclusion

The ${\rm ZrO_xN_y/V_2O_3}$ -Y nano-multilayered films were deposited with different Y additions by reactive magnetron sputtering. The microstructure and mechanical behaviors of nano-multilayered films were investigated. The conclusions are summarized as follows.

- (1) The N, Zr, and O contents in the nano-multilayered films maintain a constant at about 1.4, 26.0, and 69.9 at.%, respectively, and the V content decreases while the Y content increases with the increase of Y addition. The nano-multilayered films comprise the ZrO_2 , ZrON, ZrN, V_2O_3 , and Y_2O_3 phases.
- (2) The FWHM of nano-multilayered films initially shrinks and then expands, corresponding to the grain size increasing first and then decreasing, with the increase of Y addition. The monoclinic structure for the V₂O₃ phase and the HCP structure of the Y addition are transformed into the FCC structure of the V₂O₃-Y modulated layer and keep coherent growth with the ZrO_xN_y template layer as the Y/VO₂ ratio is 5/10.
- (3) When the Y/VO $_2$ ratio is 5/10, the maximum hardness and elastic modulus values achieve 15.1 and 182.2 GPa, respectively. The toughness of the $\rm ZrO_xN_y/V_2O_3$ -Y nano-multilayered films exhibit the same trend as the hardness, with the maximum H/E and H^3/E^2 values being 0.079 and 0.093 GPa, respectively. Meanwhile, the K_{IC} value is approximately 1.23 MPa m $^{1/2}$. It is approximately two times that of the nano-multilayered film with the Y/VO $_2$ ratio of 2/13. The incorporation of Y atoms gives rise to the phase transition, coherent interface, and dislocation movement hindrance, which affect the strengthening effect of the nano-multilayered films. The crack bridging and crack deflection enhance the fracture toughening of the $\rm ZrO_xN_y/V_2O_3$ -Y nano-multilayered films.

CRediT authorship contribution statement

Wenjie Cheng: Experimental, Formal analysis, Writing. Jingjing Wang: Formal analysis, Writing – review & editing. Ping Liu: Formal analysis, Writing – review & editing, Funding acquisition. Xun Ma: Formal analysis, Writing – review & editing. Ke Zhang: Formal analysis,

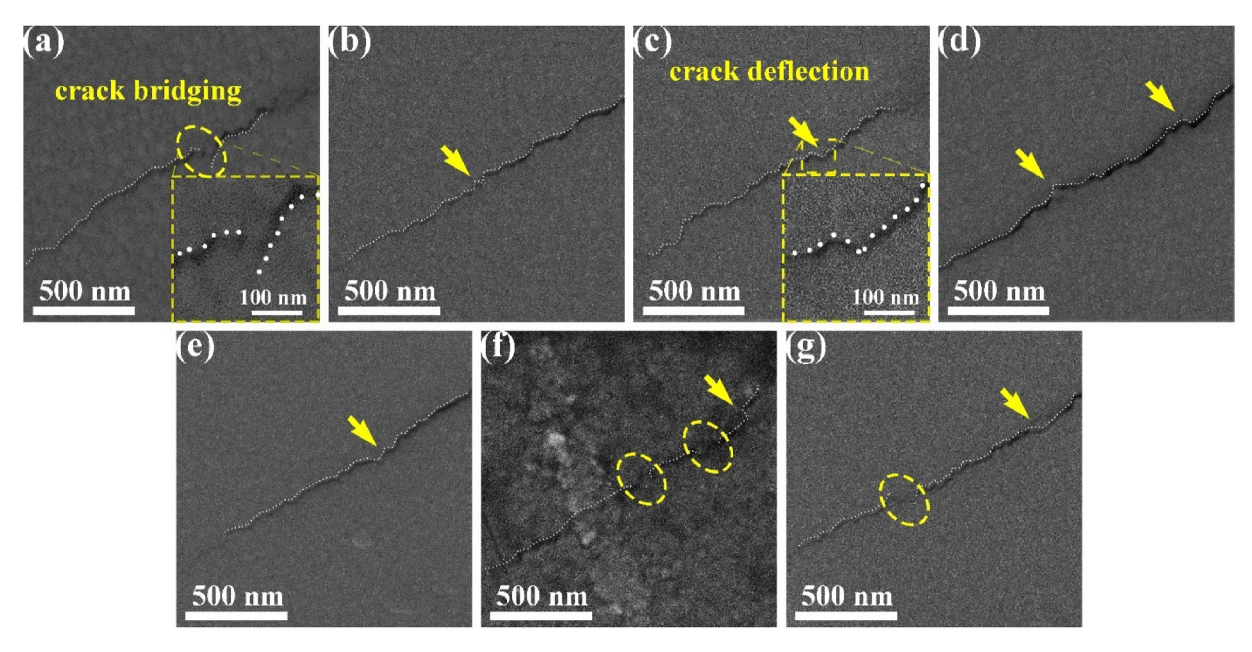


Fig. 13. Crack propagation in the ZrO_xN_y/V_2O_3 -Y nano-multilayered films with the Y/VO_2 ratio of (a) 0/15, (b) 1/14, (c) 2/13, (d) 3/12, (e) 4/11, (f) 5/10, and (g) 6/9

Writing – review & editing. **Fengcang Ma:** Formal analysis, Writing – review & editing. **Xiaohong Chen:** Formal analysis, Writing – review & editing. **Wei Li:** Formal analysis, Writing – review & editing, Supervision, Funding acquisition. **Peter K. Liaw:** Formal analysis, Writing – review & editing, Funding acquisition.

Declaration of competing interest

The authors declare that they have no known competing financial interests or personal relationships that could have appeared to influence the work reported in this paper.

Data availability

Data will be made available on request.

Acknowledgments

The present research was financially supported by the National Natural Science Foundation of China (Nos. 51971148 and 51471110), the "Dawn" Program of Shanghai Education Commission, China (No. 21SG45), the Shanghai Science and Technology Commission (22010503000) and the Shanghai Engineering Research Center of High-Performance Medical Device Materials (No. 20DZ2255500). PKL very much appreciates the supports of the U.S. Army Research Office Project (W911NF-13-1-0438 and W911NF-19-2-0049) and the National Science Foundation (DMR-1611180 and 1809640).

References

- [1] I.A. Saladukhin, G. Abadias, V.V. Uglov, S.V. Zlotski, A. Michel, A. Janse van Vuuren, Thermal stability and oxidation resistance of ZrSiN nanocomposite and ZrN/SiN_x multilayered coatings: a comparative study, Surf. Coat. Technol. 332 (2017) 428–439, https://doi.org/10.1016/j.surfcoat.2017.08.076.
- [2] Y.N. Liu, Q. Wang, J.C. Xie, X.J. Yang, P. Peng, Y. Wang, M.R. Li, C.H. Ryu, Y. H. Joo, I.W. Jeong, T.H. Sung, L.L. Xu, Enhanced surface composite coating on Ti811 alloy by laser cladding towards improved nano-hardness, Ceram. Int. 48 (2022) 18773–18783, https://doi.org/10.1016/j.ceramint.2022.03.152.
- [3] K.B. Pan, C.M. Liu, Z.C. Zhu, T.L. Feng, S.Y. Tao, B. Yang, Soft-hard segment combined carbonized polymer dots for flexible optical film with superhigh surface hardness, ACS Appl. Mater. Interfaces 14 (2022) 14504–14512, https://doi.org/ 10.1021/acsami.2c00702.

- [4] R. Psiuk, M. Milczarek, P. Jenczyk, P. Denis, D.M. Jarząbek, P. Bazarnik, M. Pisarek, T. Mościcki, Improved mechanical properties of W-Zr-B coatings deposited by hybrid RF magnetron – PLD method, Appl. Surf. Sci. 570 (2021), 151239, https://doi.org/10.1016/j.apsusc.2021.151239.
- [5] M.A. Monclús, M. Callisti, T. Polcar, L.W. Yang, J. Llorca, J.M. Molina-Aldareguía, Selective oxidation-induced strengthening of Zr/Nb nanoscale multilayers, Acta Mater. 122 (2017) 1–10, https://doi.org/10.1016/j.actamat.2016.09.021.
- [6] Z.G. Mei, S. Bhattacharya, A.M. Yacout, First-principles study of fracture toughness enhancement in transition metal nitrides, Surf. Coat. Technol. 357 (2019) 903–909, https://doi.org/10.1016/j.surfcoat.2018.10.102.
- [7] Y.Q. Xing, J.X. Deng, K.D. Zhang, X.S. Wang, Y.S. Lian, Y.H. Zhou, Fabrication and dry cutting performance of Si₃N₄/TiC ceramic tools reinforced with the PVD WS₂/ Zr soft-coatings, Ceram. Int. 41 (2015) 10261–10271, https://doi.org/10.1016/j. ceramint.2015.04.153.
- [8] A.D. Pogrebnjak, A.A. Bagdasaryan, V.M. Beresnev, U.S. Nyemchenko, V. I. Ivashchenko, Y.O. Kravchenko, Z.K. Shaimardanov, S.V. Plotnikov, O. Maksakova, The effects of Cr and Si additions and deposition conditions on the structure and properties of the (Zr-Ti-Nb)N coatings, Ceram. Int. 43 (2017) 771–782, https://doi.org/10.1016/j.ceramint.2016.10.008.
- [9] Y.M. Lei, L.N. Chen, J. Zhang, F. Xue, G.H. Bai, Y.W. Zhang, T. Liu, R. Li, S.G. Li, J. Y. Wang, Influence of Al concentration on mechanical property and oxidation behavior of Zr-Al-C coatings, Surf. Coat. Technol. 372 (2019) 65–71, https://doi.org/10.1016/j.surfcoat.2019.05.030.
- [10] A.M. Sadoun, M.M. Mohammed, E.M. Elsayed, A.F. Meselhy, O.A. El-Kady, Effect of nano Al₂O₃ coated Ag addition on the corrosion resistance and electrochemical behavior of Cu-Al₂O₃ nanocomposites, J. Mater. Res. Technol. 9 (2020) 4485–4493, https://doi.org/10.1016/j.imrt.2020.02.076.
- [11] V. Attari, A. Cruzado, R. Arroyave, Exploration of the microstructure space in TiAlZrN ultra-hard nanostructured coatings, Acta Mater. 174 (2019) 459–476, https://doi.org/10.1016/j.actamat.2019.05.047.
- [12] K. Yalamanchili, I.C. Schramm, E.J. Pique, L. Rogström, F. Mücklich, M. Oden, N. Ghafoor, Tuning hardness and fracture resistance of ZrN/Zr_{0.63}Al_{0.37}N nanoscale multilayers by stress-induced transformation toughening, Acta Mater. 89 (2015) 22–31, https://doi.org/10.1016/j.actamat.2015.01.066.
- [13] B. Bouaouina, A. Besnard, S.E. Abaidia, A. Airoudj, F. Bensouici, Correlation between mechanical and microstructural properties of molybdenum nitride thin films deposited on silicon by reactive R.F. magnetron discharge, Surf. Coat. Technol. 333 (2018) 32–38, https://doi.org/10.1016/j.surfcoat.2017.10.028.
- [14] J. Liu, B. Xu, H. Wang, X. Cui, L. Zhu, G. Jin, Effects of film thickness and icrostructures on residual stress, Surf. Eng. 32 (2016) 178–184, https://doi.org/ 10.1179/1743294415Y.0000000028.
- [15] G.A. Cheng, D.Y. Han, C.L. Liang, X.L. Wu, R.T. Zheng, Influence of residual stress on mechanical properties of TiAlN thin films, Surf. Coat. Technol. 228 (2013) 328–330, https://doi.org/10.1016/j.surfcoat.2012.05.108.
- [16] A. Rizzo, D. Valerini, L. Capodieci, L. Mirenghi, F.D. Benedetto, M.L. Protopapa, Reactive bipolar pulsed dual magnetron sputtering of ZrN films: the effect of duty cycle, Appl. Surf. Sci. 427 (2018) 994–1002, https://doi.org/10.1016/j. apsusc.2017.08.032.
- [17] J.J. Mo, Z.T. Wu, Y. Yao, Q. Zhang, Q.M. Wang, Influence of Y-addition and multilayer modulation on microstructure, oxidation resistance and corrosion behavior of Al_{0.67}Ti_{0.33}N coatings, Surf. Coat. Technol. 342 (2018) 129–136, https://doi.org/10.1016/j.surfcoat.2018.02.071.

- [18] S.Y. Liu, B.D. Ong, J. Guo, E.J. Liu, X.T. Zeng, Wear performance of Y-doped nanolayered CrN/AlN coatings, Surf. Coat. Technol. 367 (2019) 349–357, https://doi.org/10.1016/j.surfcoat.2019.02.092.
- [19] J.L. Tian, C. Hu, L. Chen, Y.M. Lou, N.N. Zhao, Structure, mechanical and thermal properties of Y-doped CrAlN coatings, Trans. Nonferrous Metals Soc. China 31 (2021) 2740–2749, https://doi.org/10.1016/S1003-6326(21)65689-3.
- [20] F. Ye, L. Zhao, C. Mu, H. Zhao, Influence of yttrium addition on reactive sputtered W-Y-N coatings, 0844, Surf. Eng. (2016), 1231758, https://doi.org/10.1080/ 02670844.2016.1231758.
- [21] Z.B. Han, L.D. Zhang, C.J. Wang, X.J. Ni, B.J. Ye, L.Q. Shi, Effects of yttrium doping on helium behavior in zirconium hydride films, Vacuum 180 (2020), 109583, https://doi.org/10.1016/j.vacuum.2020.109583.
- [22] H.L. Liang, B. Zhang, D.Y. Zhou, X.T. Guo, Y. Li, Y.Q. Lu, Y.Y. Guo, Effect of Y concentration and film thickness on microstructure and electrical properties of HfO₂ based thin films, Ceram. Int. 47 (2021) 12137–12143, https://doi.org/10.1016/j.ceramint.2021.01.060.
- [23] M. Liu, Y. Yang, Q. Mao, Y.Q. Wei, Y.J. Li, N.N. Ma, H. Liu, X.J. Liu, Z.R. Huang, Influence of radio frequency magnetron sputtering parameters on the structure and performance of SiC films, Ceram. Int. 47 (2021) 24098–24105, https://doi.org/ 10.1016/j.ceramint.2021.05.120.
- [24] J.T. Gudmundsson, N. Brenning, D. Lundin, U. Helmersson, High power impulse magnetron sputtering discharge, J. Vac. Sci. Technol.A 30 (2012), https://doi.org/ 10.1116/1.3691832, 030801–030835.
- [25] G. Betz, K. Wien, Energy and angular distributions of sputtered species, Int. J. Mass Spectrom. Ion Phys. 140 (1994) 1–110.
- [26] W.C. Oliver, G.M. Pharr, An improved technique for determining hardness and elastic modulus using load and displacement sensing indentation experiments, J. Mater. Res. 7 (1992) 1564–1583, https://doi.org/10.1557/JMR.1992.1564.
- [27] K.P. Zheng, P. Liu, W. Li, F.C. Ma, X.K. Liu, X.H. Chen, Investigation on microstructure and properties of CrAlN/AlON nanomultilayers, Appl. Surf. Sci. 257 (2011) 9583–9586, https://doi.org/10.1016/j.apsusc.2011.06.069.
- [28] A. Richel, N.P. Johnson, D.W. McComb, Observation of Bragg reflection in photonic crystals synthesized from air spheres in a titania matrix, Appl. Phys. Lett. 76 (2000) 1816–1818, https://doi.org/10.1063/1.126175.
- [29] S. Zerkout, S. Achour, N. Tabet, TiN-Fe nanocomposite thin films deposited by reactive magnetron sputtering, J. Phys. D Appl. Phys. 40 (2007) 7508–7514, https://doi.org/10.1088/0022-3727/40/23/039.
- [30] P. Ren, K. Zhang, X. He, S.X. Du, X.Y. Yang, T. An, M. Wen, W.T. Zheng, Toughness enhancement and tribochemistry of the Nb-Ag-N films actuated by solute Ag, Acta Mater. 137 (2017) 1–11, https://doi.org/10.1016/j.actamat.2017.07.034.
- [31] U. Holzwarth, N. Gibson, The Scherrer equation versus the 'Debye-Scherrer equation, Nat. Nanotechnol. 6 (2011) 145, https://doi.org/10.1038/ pnano 2011 145
- [32] Z.T. Wu, Z.T. Qi, D.T. Zhang, Z.C. Wang, Evolution of the microstructure and oxidation resistance in co-sputtered Zr-Y-N coatings, Appl. Surf. Sci. 321 (2014) 268–274, https://doi.org/10.1016/j.apsusc.2014.09.152.
- [33] W. Gulbiński, T. Suszko, Thin films of Mo₂N/Ag nanocomposite-the structure, mechanical and tribological properties, Surf. Coating. Technol. 201 (2006) 1469–1476, https://doi.org/10.1016/j.surfcoat.2006.02.017.
- [34] T. Muneshwar, K. Cadien, Comparing XPS on bare and capped ZrN films grown by plasma enhanced ALD: effect of ambient oxidation, Appl. Surf. Sci. 435 (2018) 367–376, https://doi.org/10.1016/j.apsusc.2017.11.104.
- [35] Y.O. Kravchenko, E. Coy, B. Peplińska, I. Iatsunskyi, K. Załęski, M. Kempiński, V. M. Beresnev, A.V. Pshyk, A.D. Pogrebnjak, Micro-mechanical investigation of (Al₅₀Ti₅₀)N coatings enhanced by ZrN layers in the nanolaminate architecture, Appl. Surf. Sci. 534 (2020) 147573–147584, https://doi.org/10.1016/j.apsus.2020.147573
- [36] K. Idczak, P. Mazur, S. Zuber, L. Markowski, M. Skiścim, S. Bilińska, Growth of thin zirconium and zirconium oxides films on the n-GaN(0001) surface studied by XPS and LEED, Appl. Surf. Sci. 304 (2014) 29–34, https://doi.org/10.1016/j. apsusc.2014.01.102.
- [37] F. Esaka, K. Furuya, H. Shimada, M. Imamura, N. Matsubayashi, H. Sato, A. Nishijima, A. Kawana, H. Ichimura, T. Kikuchi, Comparison of surface oxidation of titanium nitride and chromium nitride films studied by x-ray absorption and photoelectron spectroscopy, J. Vac. Sci. Technol. A 15 (1997) 2521–2528, https:// doi.org/10.1116/1.580764.
- [38] M. Matsuoka, S. Isotani, W. Sucasaire, N. Kuratani, K. Ogata, X-ray photoelectron spectroscopy analysis of zirconium nitride-like films prepared on Si(100) substrates by ion beam assisted deposition, Surf. Coat. Technol. 202 (2008) 3129–3135, https://doi.org/10.1016/j.surfcoat.2007.11.019.
- [39] V. Shapovalov, H. Metiu, VO_x (x = 1-4) submonolayers supported on rutile TiO₂(110) and CeO₂(111) surfaces: the structure, the charge of the atoms, the XPS spectrum, and the equilibrium composition in the presence of oxygen, J. Phys. Chem. C 111 (2007) 14179–14188. https://doi.org/10.1021/jn074481.
- Chem. C 111 (2007) 14179–14188, https://doi.org/10.1021/jp0744811.
 [40] D. Gu, Z.H. Sun, X. Zhou, R. Guo, T. Wang, Y.D. Jiang, Effect of yttrium-doping on the microstructures and semiconductor-metal phase transition characteristics of polycrystalline VO₂ thin films, Appl. Surf. Sci. 359 (2015) 819–825, https://doi.org/10.1016/j.apsusc.2015.10.179.
- [41] Z.B. Han, G.J. Cheng, L.Q. Shi, Synthesis and characterization of Y-doped TiH₂ films prepared by magnetron sputtering, Int. J. Hydrogen Energy 41 (2016) 2820–2828, https://doi.org/10.1016/j.ijhydene.2015.12.127.
- [42] P.P. Cui, W. Li, P. Liu, K. Zhang, F.C. Ma, X.H. Chen, R. Feng, P.K. Liaw, Effects of nitrogen content on microstructures and mechanical properties of (AlCrTiZrHf)N high-entropy alloy nitride films, J. Alloys Compd. 834 (2020), 155063, https://doi. org/10.1016/j.jallcom.2020.155063.

- [43] M.K. Liu, H.Y. Hwang, H. Tao, A.C. Strikwerda, K.B. Fan, G.R. Keiser, A. J. Sternbach, K.G. West, S. Kittiwatanakul, J.W. Lu, S.A. Wolf, F.G. Omenetto, X. Zhang, K.A. Nelson, R.D. Averitt, Terahertz-field-induced insulator-to-metal transition in vanadium dioxide metamaterial, Nature 487 (2012) 345–348, https://doi.org/10.1038/nature11231.
- [44] J. Yoon, H. Kim, X. Chen, N. Tamura, B.S. Mun, C. Park, H. Ju, Controlling the temperature and speed of the phase transition of VO₂ microcrystals, ACS Appl. Mater. Interfaces 8 (2016) 2280–2286, https://doi.org/10.1021/acsami.5b11144
- [45] W.H. Haw, H.H. Jia, G.P. Yu, Effect of oxygen on fracture toughness of Zr(N,O) hard coatings, Surf. Coat. Technol. 304 (2016) 330–339, https://doi.org/10.1016/ i.surfcoat.2016.07.026.
- [46] Y.E. Ke, Y.I. Chen, Effects of nitrogen flow ratio on structures, bonding characteristics, and mechanical properties of ZrN_x films, Coatings 10 (2020) 476–488, https://doi.org/10.3390/coatings10050476.
- [47] H.M. Du, P. Liu, W. Li, K. Zhang, F.C. Ma, X.K. Liu, X.H. Chen, D.H. He, Al₈₀Cr₂₀N-layer thickness-dependent microstructure and mechanical properties of Al₅₀Cr₅₀N/Al₈₀Cr₂₀N nanomultilayered films, Vacuum 162 (2019) 1–7, https://doi.org/10.1016/j.vacuum.2019.01.017.
- [48] W. Li, P. Liu, K. Zhang, F.C. Ma, X.K. Liu, X.H. Chen, D.H. He, Structural evolution of yttrium nanolayer inserted in FeNi/Y nanomultilayered film, Appl. Surf. Sci. 317 (2014) 935–939, https://doi.org/10.1016/j.apsusc.2014.09.010.
- [49] J. Buchinger, N. Koutná, Z. Chen, Z. Zhang, P.H. Mayrhofer, D. Holec, M. Bartosik, Toughness enhancement in TiN/WN superlattice thin films, Acta Mater. 172 (2019) 18–29, https://doi.org/10.1016/j.actamat.2019.04.028.
- [50] Y.X. Xu, L. Chen, F. Pei, K.K. Chang, Y. Du, Effect of the modulation ratio on the interface structure of TiAlN/TiN and TiAlN/ZrN multilayers: first-principles and experimental investigations, Acta Mater. 130 (2017) 281–288, https://doi.org/ 10.1016/j.actamat.2017.03.053.
- [51] Y. Chen, T. Guo, J. Wang, X. Pang, L. Qiao, Effects of orientation on microstructure and mechanical properties of TiN/AlN superlattice films, Scripta Mater. 201 (2021), 113951, https://doi.org/10.1016/j.scriptamat.2021.113951.
- [52] D. Liu, C.F. Ruan, P. Zhang, H. Ma, Y. Liang, J. Tu, Structural, interface texture and toughness of TiAlN/CNx multilayer films, Mater. Char. 178 (2021), https://doi. org/10.1016/j.matchar.2021.111301.
- [53] A.V. Pshyk, L.E. Coy, G. Nowaczyk, M. Kempiński, B. Peplińska, A.D. Pogrebnjak, V.M. Beresnev, S. Jurga, High temperature behavior of functional TiAlBSiN nanocomposite coatings, Surf. Coating. Technol. 305 (2016) 49–61, https://doi. org/10.1016/j.surfcoat.2016.07.075.
- [54] P. Ren, K. Zhang, M. Wen, S.X. Du, J.H. Chen, W.T. Zheng, The roles of Ag layers in regulating strengthening-toughening behavior and tribochemistry of the Ag/TaC nano-multilayer films, Appl. Surf. Sci. 445 (2018) 415–423, https://doi.org/ 10.1016/j.apsusc.2018.03.202.
- [55] Y. Kong, X.B. Tian, C.Z. Gong, P.K. Chu, Enhancement of toughness and wear resistance by CrN/CrCN multilayered coatings for wood processing, Surf. Coat. Technol. 344 (2018) 204–213. https://doi.org/10.1016/j.surfcoat.2018.03.027.
- [56] J.S. Koehler, Attempt to design a strong solid, Phys. Rev. B 2 (1970) 547–551, https://doi.org/10.1103/PhysRevB.2.547.
- [57] P.M. Anderson, C. Li, Hall-Petch realstions for multilayered materials, Nanostruct. Mater. 5 (1995) 349–362. https://doi.org/10.1016/0965-9773(95)00250-1
- Mater. 5 (1995) 349–362, https://doi.org/10.1016/0965-9773(95)00250-I.
 [58] G.Y. Li, Z.H. Han, J.W. Tian, J.H. Xu, M.Y. Gu, Alternating stress field and superhardness effect in TiN/NbN superlattice films, J. Vac. Sci. Technol.A 20 (2002) 674–677, https://doi.org/10.1116/1.1460887.
- [59] Q. Zhang, X. Wu, S. Qin, Pressure-induced phase transition of V_2O_3 , Chin. Phys. Lett. 29 (2012) 2–5, https://doi.org/10.1088/0256-307X/29/10/106101.
- [60] A. Tishin, S. Nikitin, V.Y. Bodriakov, Young's modulus and internal friction of yttrium, J. Phys. I. 5 (1995) 525–532, https://doi.org/10.1051/jp1:1995145.jpa-00247077.
- [61] B.R. Lawn, A.G. Evans, D.B. Marshall, Elastic/plastic indentation damage in ceramics: the median/radial crack system, J. Am. Ceram. Soc. 63 (1980) 574–581, https://doi.org/10.1111/j.1151-2916.1980.tb10768.x.
- [62] J.M. Jungk, B.L. Boyce, T.E. Buchheit, T.A. Friedmann, D. Yang, W.W. Gerberich, Indentation fracture toughness and acoustic energy release in tetrahedral amorphous carbon diamond-like thin films, Acta Mater. 54 (2006) 4043–4052, https://doi.org/10.1016/j.actamat.2006.05.003.
- [63] C.Y. Yen, S.R. Jian, Y.C. Tseng, J.Y. Juang, The deformation behavior and fracture toughness of single crystal YSZ(111) by indentation, J. Alloys Compd. 735 (2018) 2423–2427, https://doi.org/10.1016/j.jallcom.2017.12.022.
- [64] W.J. Cheng, W. Li, J.J. Wang, P. Liu, X. Ma, K. Zhang, F.C. Ma, X.H. Chen, P. K. Liaw, Effects of N₂/Ar flow ratio on the structures and mechanical behavior of ZrO_xN_y/V₂O₃ nano-multilayered films, Mater. Sci. Eng. 849 (2022), 143419, https://doi.org/10.1016/j.msea.2022.143419.
- [65] C. Kainz, N. Schalk, M. Tkadletz, C. Mitterer, C. Czettl, Microstructure and mechanical properties of CVD TiN/TiBN multilayer coatings, Surf. Coating. Technol. 370 (2019) 311–319, https://doi.org/10.1016/j.surfcoat.2019.04.086.
- [66] Z. Guo, D. Ma, X. Zhang, J. Li, J. Feng, Preparation and toughening of a-CuZr/c-ZrN nano-multilayer hard coatings, Appl. Surf. Sci. 483 (2019) 432–441, https://doi.org/10.1016/j.apsusc.2019.03.289.
- [67] Y.H. Ma, Z.G. Wang, J.H. Ouyang, S.J. Dillon, A. Henniche, Y.H. Wang, Y.J. Wang, Microstructural toughening mechanisms in nanostructured Al₂O₃/GdAlO₃ eutectic composite studied using in situ microscale fracture experiments, J. Eur. Ceram. Soc. 40 (2020) 3148–3157, https://doi.org/10.1016/j.jeurceramsoc.2020.02.042.
- [68] M.D. Yi, G.Q. Jing, D.P. Li, G.C. Xiao, Z.Q. Chen, J.J. Zhang, L. Wang, C.H. Xu, Strengthening and toughening mechanism of (W,Ti,Ta)C based cermet with the addition of c-BN@Al2O3, Ceram. Int. 47 (2021) 32075–32085, https://doi.org/ 10.1016/j.ceramint.2021.08.097.

- [69] R. Daniel, M. Meindlhumer, W. Baumegger, J. Zalesak, B. Sartory, M. Burghammer, C. Mitterer, J. Keckes, Grain boundary design of thin films: using tilted brittle interfaces for multiple crack deflection toughening, Acta Mater. 122 (2017) 130–137, https://doi.org/10.1016/j.actamat.2016.09.027.
 [70] J.L. Chai, Y. Bin Zhu, T.L. Shen, Y.W. Liu, L.J. Niu, S.F. Li, P. Jin, M.H. Cui, Z.
- [70] J.L. Chai, Y. Bin Zhu, T.L. Shen, Y.W. Liu, L.J. Niu, S.F. Li, P. Jin, M.H. Cui, Z. G. Wang, Assessing fracture toughness in sintered Al₂O₃–ZrO₂(3Y)–SiC ceramic composites through indentation technique, Ceram. Int. 46 (2020) 27143–27149, https://doi.org/10.1016/j.ceramint.2020.07.194.
- [71] B.L. Ye, T.Q. Wen, M.C. Nguyen, L.Y. Hao, C.Z. Wang, Y.H. Chu, First-principles study, fabrication and characterization of (Zr_{0.25}Nb_{0.25}Ti_{0.25}V_{0.25})C high-entropy ceramics, Acta Mater. 170 (2019) 15–23, https://doi.org/10.1016/j. actamat.2019.03.021.
- [72] S.H. Zhou, T.C. Kuang, Z.G. Qiu, D.C. Zeng, K.S. Zhou, Microstructural origins of high hardness and toughness in cathodic arc evaporated Cr-Al-N coatings, Appl. Surf. Sci. 493 (2019) 1067–1073, https://doi.org/10.1016/j.apsusc.2019.07.051.